Bose-Einstein condensation in honeycomb dimer magnets and $Yb_2Si_2O_7$

Chunhan Feng [1,2] E. Miles Stoudenmire,[1] and Alexander Wietek[3,1]

[1]*Center for Computational Quantum Physics, Flatiron Institute, New York, New York 10010, USA*
[2]*Department of Physics, University of California, Davis, California 95616, USA*
[3]*Max Planck Institute for the Physics of Complex Systems, Nöthnitzer Strasse 38, Dresden 01187, Germany*

An asymmetric Bose-Einstein condensation (BEC) dome was observed in a recent experiment on the quantum dimer magnet $Yb_2Si_2O_7$e [G. Hester *et al.*, Phys. Rev. Lett. **123**, 027201 (2019)], which is modeled by a "breathing" honeycomb lattice Heisenberg model with possible anisotropies. We report a remarkable agreement between key experimental features and predictions from numerical simulations of the magnetic model. Both critical fields, as well as critical temperatures of the BEC dome, can be accurately captured, as well as the occurrence of two regimes inside the BEC phase. Furthermore, we investigate the role of anisotropies in the exchange coupling and the g tensor. While we confirm a previous proposal that anisotropy can induce a zero-temperature phase transition at magnetic fields smaller than the fully polarizing field strength, we find that this effect becomes negligible at temperatures above the anisotropy scale. Instead, the two regimes inside the BEC dome are found to be due to a nonlinear magnetization behavior of the isotropic breathing honeycomb Heisenberg antiferromagnet. Our analysis is performed by combining the density matrix renormalization group (DMRG) method with the finite-temperature techniques of minimally entangled typical thermal states (METTS) and quantum Monte Carlo (QMC).

I. INTRODUCTION

Quantum magnets exhibit many phenomena, which currently elude our understanding [1–3]. The combination of quantum and thermal fluctuations of local magnetic moments combined with possible geometric frustration can lead to the emergence of entirely new states of matter. As computational methods for quantum many body systems have significantly advanced in recent years [4–6], the bridge between experimental observations and explanations using theoretical models can increasingly be built not only on a qualitative, but also quantitative level.

A particularly interesting phenomenon in quantum magnetism is the Bose-Einstein condensation of triplons in quantum dimer magnets [2,7]. A broad variety of compounds have to date been found to exhibit this magnetic analogue of superfluidity in ^{4}He, including $BaCuSi_2O_6$ [8–10], $TlCuCl_3$ [11–13], and $Ba_3Cr_2O_8$ [14–16]. Here the magnetic field acts as the chemical potential condensing the bosonic triplons, which are the elementary excitations of the local spin-singlet dimers. This condensation at a critical value of the magnetic field H_{c_1} causes the system to order antiferromagnetically at low temperatures, before reaching a fully spin-polarized state beyond a larger critical magnetic field H_{c_2}. The intervening antiferromagnetic or BEC phase forms a dome in the temperature vs field phase diagram, the maximum temperature of this dome ranging from a few hundred milli-Kelvin to around 10 Kelvin depending on the compound. Typical values of H_{c_1} and H_{c_2} range from 1 to 100 Tesla.

Conventionally, the BEC dome constitutes a single phase of matter. But surprisingly, recent experimental results on the material $Yb_2Si_2O_7$ [17] discovered two distinct regimes separated by another field value H_m between the H_{c_1} and H_{c_2} fields inside the BEC dome of this compound. The critical magnetic fields $H_{c_1} \approx 0.4$T and $H_{c_2} \approx 1.4$T have been found to be low compared to similar quantum dimer magnets [17]. The two regimes are distinguished by a change in the field dependence of the magnetization and the related ultrasound velocity. Moreover, the regime at smaller magnetic fields features a sharp anomaly in the specific heat, which is absent in the larger field regime. The magnetic properties of this compound can be modeled by a "breathing" honeycomb antiferromagnet. To explain the peculiar features observed in experiment, a recent paper has highlighted the role of anisotropies in both the spin exchange as well as the g tensor [18]. Here, we extend this analysis to study the full finite-temperature phase diagram of the model proposed in Ref. [18]. We establish critical fields and temperatures of the BEC phase as well as the existence of two regimes inside the BEC dome signalled by a change in the behavior of the magnetization process. A particular focus will be on the role of possible anisotropies at finite temperature.

II. MODEL AND METHODOLOGY

We study a "breathing" Heisenberg antiferromagnetic with additional anisotropies model previously proposed in Refs. [17,18], given by

$$\mathcal{H} = \sum_{\langle \mathbf{i},\mathbf{j} \rangle, \alpha} J_{\mathbf{ij}}^{\alpha} S_{\mathbf{i}}^{\alpha} S_{\mathbf{j}}^{\alpha} - H \sum_{\mathbf{i},\alpha} g_{z\alpha} S_{\mathbf{i}}^{\alpha}, \tag{1}$$

where $\mathbf{i}, \mathbf{j}$ are lattice sites, $\langle \mathbf{i}, \mathbf{j} \rangle$ denotes the nearest neighbors on a honeycomb lattice and $\alpha = x, y, z$ indicates the spin directions. A breathing honeycomb lattice is shown
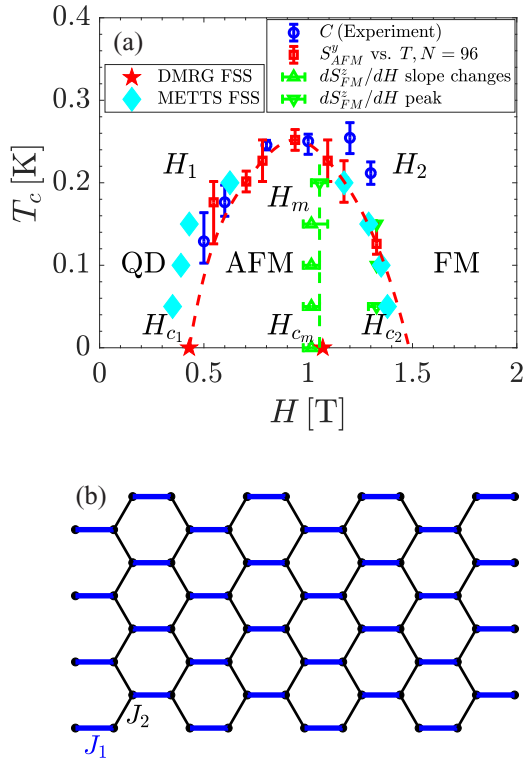
FIG. 1. (a) Phase diagram: Critical temperature T_c (Kelvin) vs magnetic field H (Tesla). The blue circles are the peak positions of heat capacity C vs temperature T from the experiment [17], while red squares are obtained by locating the largest slope points in S_{AFM}^y vs T for a Z4_12 system with $N = 96$ sites. Green upper triangles (the vertical dashed line inside the dome) indicate the slope changes in dS_{FM}^z/dH on a Z4_16 honeycomb lattice with $N = 128$ sites, related to an analogous shift in the ferromagnetic Bragg peak and the ultrasound velocity in experiment. The green down triangles are the peak position of dS_{FM}^z/dH vs H at different temperatures. The red dashed curve is only a guide to the eye. A finite-size scaling analysis is also conducted to obtain the crossings, which are revealed by red stars (for the ground state using DMRG data) and cyan diamonds (for finite temperatures using METTS data). (b) Geometry of a ZW_L simulation cylinder with $W = 4$ and $L = 8$. W refers to the width (y-direction size) of the cylinder and L to the length (x-direction size). The total number of sites of a "ZW_L" system is N $= 2 \times$ W $\times$ L. We use periodic boundary condition (PBC) for y direction and open boundary condition (OBC) for x direction.

in Fig. 1(a). The couplings J_1 on blue horizontal bonds are stronger than couplings J_2 on the remaining nearest-neighbor bonds, $J_1 > J_2$. In the limit $J_2 = 0$, the ground state is a product of local singlets on the dimers. In experiments [17], the coupling constants have been estimated to be $J_1 = 0.217(3)$ meV and $J_2 = 0.089(1)$ meV, corresponding to a ratio of $J_2/J_1 = 0.41003221$. Similar to Ref. [18], we consider a spin anisotropy by setting $J_{ij}^y = (1 + \lambda)J_{ij}^x$, $J_{ij}^z = J_{ij}^x = J_1$, resp. J_2, and $\lambda = 0.03$. Such a small λ guarantees the physics can be mainly characterized by the Heisenberg model. This spin anisotropy breaks the spin SU(2) rotations symmetry down to a remaining U(1) symmetry with the Y axis as a principal axis of rotation. A further anisotropy is introduced by a nonisotropic g tensor. We consider $g_{zy} = 0$, and a

staggered coupling in X direction is used $|g_{zx}| = g_{zz}/500$, $g_{zx}^A = -g_{zx}^B$ for sublattice A and B. This additional anisotropy further breaks down the U(1) symmetry to a remaining $\mathbf{Z}_2$ symmetry for $H \neq 0$. To emphasize how closely the experiments on $Yb_2Si_2O_7$ are captured by our results, all results in this paper are reported in experimental units, set by $J_1 = 0.217(3)$ meV, $J_2 = 0.089(1)$ meV, and $g_{zz} = 4.8$.

To study the system with Hamiltonian Eq. (1) we use three numerical methods. For zero-temperature properties we use the DMRG algorithm [19,20]. For properties at a finite temperature T, we use the minimally entangled typical thermal states (METTS) approach [6,21–24]. Both these methods are implemented using the ITensor software (C++ version) [25].

The METTS algorithm samples a set of quantum states whose average yields controlled finite-temperature results. Unlike quantum Monte Carlo methods, METTS does not encounter sign or complex phase problems that would occur in our model Eq. (1) from the magnetic field term coupling to multiple spin components. The METTS algorithm is motivated as follows: The expectation value of an observable $\mathcal{O}$ can be expressed as

$$\langle \mathcal{O} \rangle_\beta = \frac{1}{\mathcal{Z}} \text{Tr}[e^{-\beta H} \mathcal{O}]$$

$$= \frac{1}{\mathcal{Z}} \sum_i \langle i | e^{-\beta H/2} \mathcal{O} e^{-\beta H/2} | i \rangle \quad (2)$$

$$= \frac{1}{\mathcal{Z}} \sum_i P(i) \langle \phi(i) | \mathcal{O} | \phi(i) \rangle, \quad (3)$$

where

$$|\phi(i)\rangle = P(i)^{-1/2} e^{-\beta H/2} |i\rangle \quad (4)$$

$$P(i) = \langle i | e^{-\beta H} | i \rangle. \quad (5)$$

Here $\mathcal{Z}$ is the partition function and $|i\rangle$ is an orthonormal basis of classical product states. The states $|\phi(i)\rangle$ are known as METTS. To calculate $|\phi(i)\rangle$, we use matrix product states (MPS) to evolve the states $|i\rangle$ in imaginary time, using a combination of Trotter gates and the TDVP algorithm to perform the time evolution [23,26]. We also take advantage of the METTS pure state algorithm in our simulations, constructing the next METTS from a product state obtained by collapsing the previous METTS, which guarantees quantum states are sampled efficiently with the desired distribution. The maximum bond dimension required to use a MPS to represent the state increases exponentially in the width of two-dimensional lattices hence we restrict the width of the honeycomb lattice to be four in this paper. The typical maximum bond dimension we set is 500 and the truncation error cutoff is 10^{-6}, which sets the actual bond dimension used in this paper. Finally, for studying the isotropic case where $\lambda = 0$ and $g_{zx} = g_{xz} = 0$ we employ quantum Monte Carlo simulations in the form of the worm algorithm [27,28].

III. PHASE DIAGRAM

The main result of this paper is a temperature T_c [K] vs magnetic field H [T] phase diagram shown in Fig. 1. We will use H_{c_1}, H_{c_m}, H_{c_2} to represent the critical magnetic fields in

the ground state and H_1, H_m, H_2 at finite temperatures. We determine the phase boundaries several different ways: (1) We conduct a finite-size scaling analysis for the antiferromagnetic (AFM) structure factor S_{AFM}^y for spin y in the ground state given by DMRG (red stars, H_{c_1} and H_{c_m}) and at finite temperatures obtained by METTS (cyan diamonds, H_1 and H_2). We use the crossings of rescaled S_{AFM}^y for different system sizes to locate the transitions. (2) For different magnetic fields H, we locate the temperature T^* (red squares) at which S_{AFM}^y vs T curves have the largest slope. (3) We compute the derivative of the ferromagnetic structure factor for the spin z component with respect to magnetic field, dS_{FM}^z/dH, which is the derivative of the magnetic Bragg peak intensity (proportional to the square of net magnetization) with respect to magnetic field in the experiment, which behaves analogously to the ultrasound velocity [17]. Magnetic field values H_m where the slope of the curves changes significantly are shown as green triangles along the vertical dashed line in Fig. 1. The peak positions H_2 in dS_{FM}^z/dH vs H are denoted by green down triangles along the right boundary of the dome.

The phase diagram given by the heat capacity in the experiment is also shown as blue circles in Fig. 1 as a comparison to our simulations. All these approaches of obtaining the transition points will be discussed in more detail in the following sections.

IV. GROUND-STATE PROPERTIES

We perform DMRG calculations to study the ground-state physics of the system and verified the results presented in [18]. We investigate the magnetic structure factor,

$$S^\alpha(\mathbf{q}) = \frac{1}{N} \sum_{\mathbf{i},\mathbf{j}} \langle S_{\mathbf{i}}^\alpha S_{\mathbf{j}}^\alpha \rangle e^{i\mathbf{q}\cdot(\mathbf{i}-\mathbf{j})}, \quad (6)$$

where N is the total number of sites and $\mathbf{q}$ denotes the momentum. Results on various system sizes are shown in Fig. 2. We investigate both the ferromagnetic (FM) and antiferromagnetic (AFM) structure factors, $S_{FM}^\alpha = S^\alpha(\mathbf{q} = (0,0))$ and $S_{AFM}^\alpha = S^\alpha(\mathbf{q} = M)$. When the external magnetic field is relatively small, $H \lesssim H_{c_1} \sim 0.43$ T, the ground state is in the singlet quantum dimer phase, adiabatically connected to a product state of singlet dimers. Thus, S_{FM}^α vanishes but S_{AFM}^α retains a finite value. In the middle of the dome, S_{AFM}^y increases to its maximum at around $H \sim 0.8$ T and then decreases. In the ordered AFM phase, S_{AFM}^y is roughly proportional to the lattice size N, indicating a long-range order has developed. When $H \gtrsim 1.5$ T, the ground state is the spin polarized phase. S_{AFM}^α vanishes and S_{FM}^z retains a finite value.

In order to locate the transition magnetic field H_{c_1} and H_{c_m} more accurately, we conduct a finite-size scaling analysis. Since a nonzero $g_{zx} = 1/500$ introduces a tiny staggered magnetic field in spin x direction, the AFM pattern in the x spin component is a consequence of the field rather than a spontaneous symmetry breaking. Therefore to investigate spontaneous symmetry breaking and phase transitions we focus only on AFM order in the spin y direction.

When $H_{c_1} < h < H_{c_m}$ the ground state breaks a $\mathbb{Z}_2$ symmetry. Thus, we may expect that the magnetic transition exhibits universal finite-size scaling of S_{AFM}^y described by the
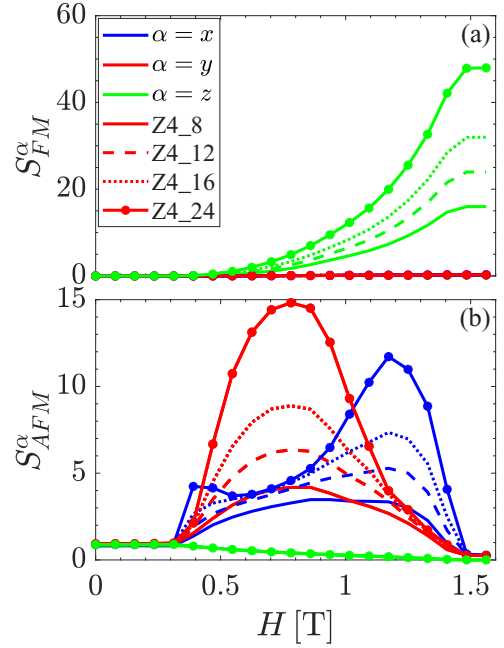

FIG. 2. Ferromagnetic and antiferromagnetic structure factors S_{FM}, S_{AFM} vs magnetic field H for different spin $\sigma = x, y, z$ components. Different line types represent the results for different lattice sizes.

2D Ising critical exponents $\beta = 1/8$ and $\nu = 1$. The rescaled AFM structure factor $S_{AFM}^y/L^{1-2\beta/\nu}$ is plotted as a function of magnetic field H in Fig. 3. The two crossing points appearing in the plot indicate $H_{c_1} \sim 0.43$ T and $H_{c_m} \sim 1.07$ T, which is in agreement with [18]. When $H_{c_1} \lesssim H \lesssim H_{c_m}$, AFM order appears in both spin x and y, while a long range AFM order in spin y vanishes and the order in x dominates when $H_{c_m} \lesssim H \lesssim H_{c_2}$.

V. FINITE TEMPERATURE PROPERTIES

After verifying the ground state phase diagram, we move to finite temperature properties, which are the main focus of
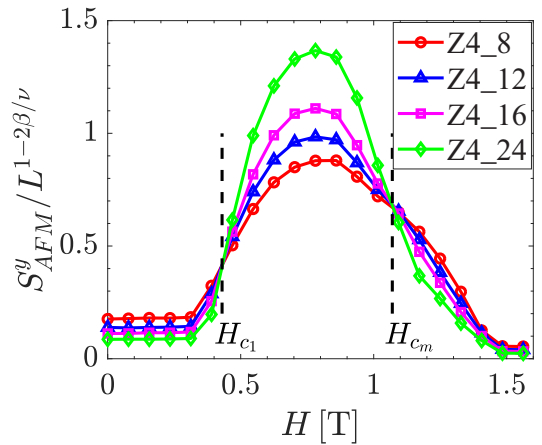

FIG. 3. Finite-size scaling analysis for antiferromagnetic structure factor (spin y component) S_{AFM}^y. $\beta = 1/8$, $\nu = 1$ are 2D Ising critical exponents. The two crossing points in the plot indicate $H_{c_1} \sim 0.43$ T and $H_{c_m} \sim 1.07$ T.
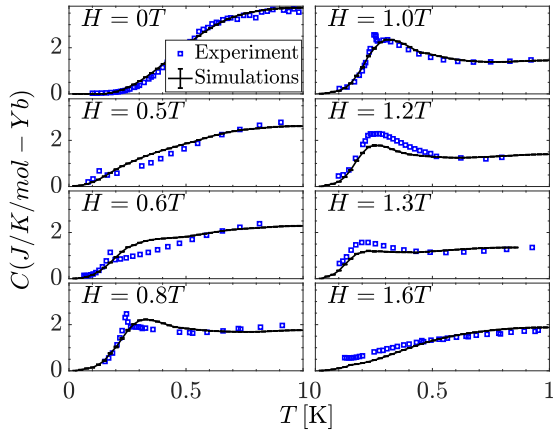
FIG. 4. Heat capacity C as a function of temperature T for several different magnetic field H on the Z4_12. At $H = 0$ T, the system is in the quantum dimer phase and heat capacity displays a broad Schottky peak at $T \sim 1$ K. The system transits to AFM phase when 0.5 T $\lesssim$ H $\lesssim 1.0$ T, and a sharp peak is observed. In this region, the transition temperature T_c increases as magnetic field goes up. When magnetic field further increases, $H \sim 1.2 - 1.3$ T, T_c descends with H increasing, tracking the right-hand side of the BEC dome. When $H \sim 1.6$ T or higher, the broad peak shifts to higher temperatures in the polarized phase as expected.

this paper. The heat capacity $C = dE/dT$ [J/K/(mol − Yb)] vs temperature T [K] for several different magnetic fields is shown in Fig. 4. The simulation results (solid black curve) match with the experiment data (blue dots) reasonably well, especially considering the limited system sizes used in the METTS calculations. In the absence of magnetic field, specific heat exhibits a broad maximum at ~1 K. When 0.5 T $\lesssim$ H $\lesssim 1.0$T a sharp anomaly is observed in the experiment indicating a transition to a long range AF order existing in the system, which will be further verified by investigating magnetic structure factors. The transition temperature T_c goes up as the magnetic field H increases from 0.5 T to 1.0 T. This maps out the left boundary of the BEC dome in the H vs T phase diagram. Although the peaks in heat capacity curves given by simulations are not as sharp as those in experiments, possibly due to the finite lattice size effect or other type of interactions in real materials, which cannot be fully characterised by the Hamiltonian, the positions of the peaks and the main feature of the curves can still be reflected by simulations.

When H further grows up to 0.8 T, a broad feature is noticed in the curve and dominates above H_{c_m}. The location of the heat capacity peak moves to lower temperatures when the magnetic field further increases. This corresponds to the phase boundary H_2 of the high magnetic field region of the dome. It describes a transition from AF order to a fully polarized paramagnetic phase. As expected, in the paramagnetic phase, $H \gtrsim H_{c_2} \sim 1.4$ T the broad peak shifts to higher temperatures as magnetic field increases.

Similar to our previous ground-state study, we explore the FM and AFM structure factors for finite temperatures as well. The spin y antiferromagnetic structure factor S^y_{AFM} is examined as a function of the magnetic field H in Fig. 5(a). In the quantum dimer or singlet phase, $H \lesssim H_1 \sim 0.43$ T, S^y_{AFM} has a finite value. When $H_1 \lesssim H \lesssim H_2$, a dome appears
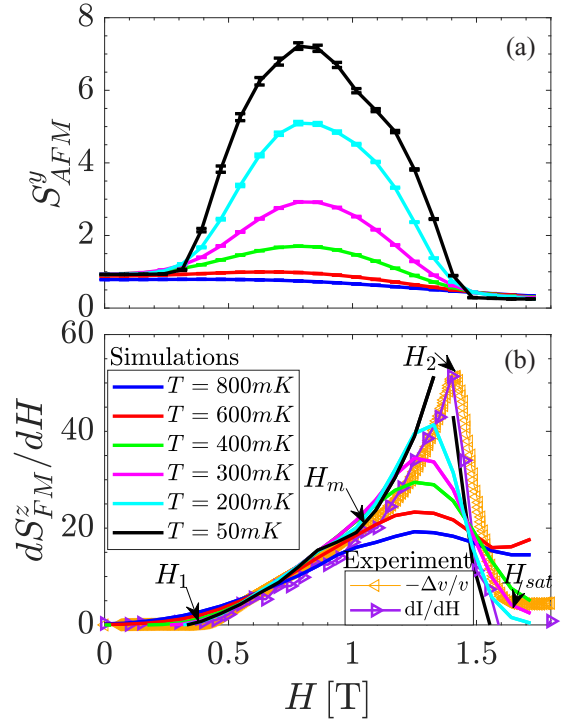

FIG. 5. (a) Antiferromagnetic structure factor for spin Y, S^y_{AFM} as a function of magnetic field H (Tesla). (b) The derivative of ferromagnetic structure factor for spin Z S^z_{FM} as a function of magnetic field H (Tesla) for "Z4_12" system. The inverse of the ultrasound velocity $-\Delta v/v$ and the derivative of the Bragg peak intensity dI/dH at $T = 50$ mK, obtained in experiment [17] are shown in orange and purple lines respectively as comparisons. The peak value of these experiment data are rescaled to match the maximum of our simulation results.

in S^y_{AFM} vs H, indicating the AFM order in spin Y develops. The magnitude of the structure factor goes up as temperature decreases as expected. When the magnetic field becomes relatively large, spins tend to be in the same direction as the magnetic field. The FM order in the spin Z component is observed and S^y_{AFM} almost vanishes as $H \gtrsim H_2$. We take the derivative of S^y_{AFM} with respect to H to locate the largest slope position H^* and mark them by red squares in the phase diagram Fig. 1. Although this cannot be viewed as an accurate method to determine the phase transition points, it can give us a rough estimate of the phase boundary of the BEC dome, inside which AFM order develops.

In addition, the derivative of ferromagnetic structure factor in spin Z with respect to magnetic field dS^z_{FM}/dH, is plotted as a function of H in Fig. 5(b). It is the derivative of Bragg peak intensity, which behaves similar to the ultrasound velocity in the experiment [17]. dS^z_{FM}/dH is almost 0 when $H \lesssim H_{c_1} \sim 0.43$ T. A significant slope change occurs at $H_m \sim 1.07$ T at low temperatures and we denote these points by green triangles in Fig. 1. This change in slope was highlighted in experiment as a main indication of the occurrence of two regimes. The positions of the peak correspond to $H_2 \sim 1.4$ T, denoted by green down triangles in Fig. 1. When $H \gtrsim 1.6$ T, S^z_{FM} saturates and hence dS^z_{FM}/dH goes down to and stays at a value close to 0 at low temperatures.
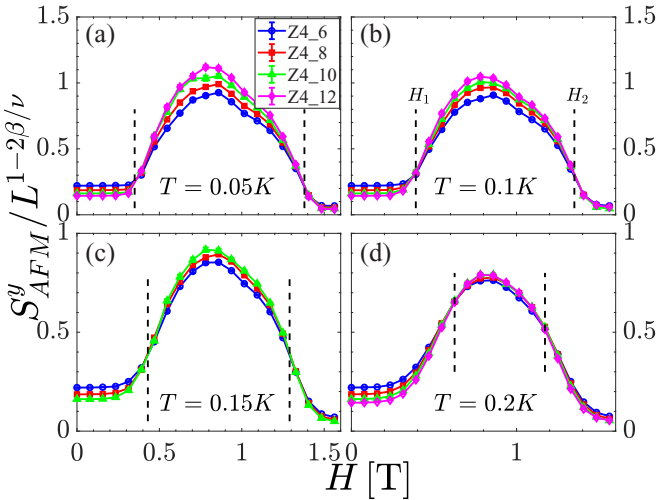
FIG. 6. Finite-size scaling analysis: Rescaled antiferromagnetic structure factor $S_{\text{AFM}}^y / L^{1-2\beta/\nu}$ vs magnetic field H [T] for several different temperatures. 2D Ising critical exponents $\beta = 1/8$, $\nu = 1$ are used. The two crossings in each plot at different temperatures T, H_1(left) and H_2(right) are denoted by cyan diamonds in Fig. 1.

In order to give a more accurate value for the transition out of the ordered phase at larger fields, we apply finite-size scaling analysis to the system at several temperatures, $T = 0.05, 0.1, 0.15, 0.2$ K in Fig. 6. Since the order breaks a Z_2 symmetry, we fit to a scaling form using the 2D Ising critical exponents $\beta = 1/8$, $\nu = 1$ [29–32]. Two crossing points H_1 and H_2 are observed as expected. We present these data points by cyan diamonds in Fig. 1. These points basically follow the boundary of the BEC dome instead of locating at the green dashed line around $H_{c_m} \sim 1.07$ T. This suggests the "intermediate" order in the ground state found in [18]—which was attributed to a nonzero value of g_{zx}—is in fact quickly washed out as temperature T increases such that the transition point likely moves rapidly from $H_{c_m} \sim 1.07$ T at $T = 0$ K (red star) to $H_2 \sim 1.4$ T at $T = 0.05$ K (cyan diamond). Although this "intermediate phase" therefore disappears at finite T, the slope changes in dS_{FM}^z/dH discussed above can still be observed, implying the similar phenomena observed in ultrasound velocity in the experiment at H_{c_m} is more likely due to a crossover rather than a phase transition. More evidence to support this argument will be shown in the texts and plots below, where we will see that it is a very general feature and rather insensitive to details such as the value of g_{zx}.

VI. THE ISOTROPIC MODEL

As is discussed in Sec. V, the critical magnetic field indicated by the second crossing point in the finite-size scaling analysis moves quickly from $H_{c_m} \sim 1.07$ T in the ground state to $H_2 \sim 1.4$ T at a small temperature $T = 0.05$ K, implying the tiny staggered magnetic field in the spin x direction (small g_{zx} value) might not be the correct explanation of the feature at H_{c_m} shown as a vertical green dashed line in Fig. 1. Hence, we employ simulations for $g_{zx} = 0$ in this section and compare them with results in Secs. V, IV with $g_{zx} = 1/500$ to explore the true effects of g_{zx}.
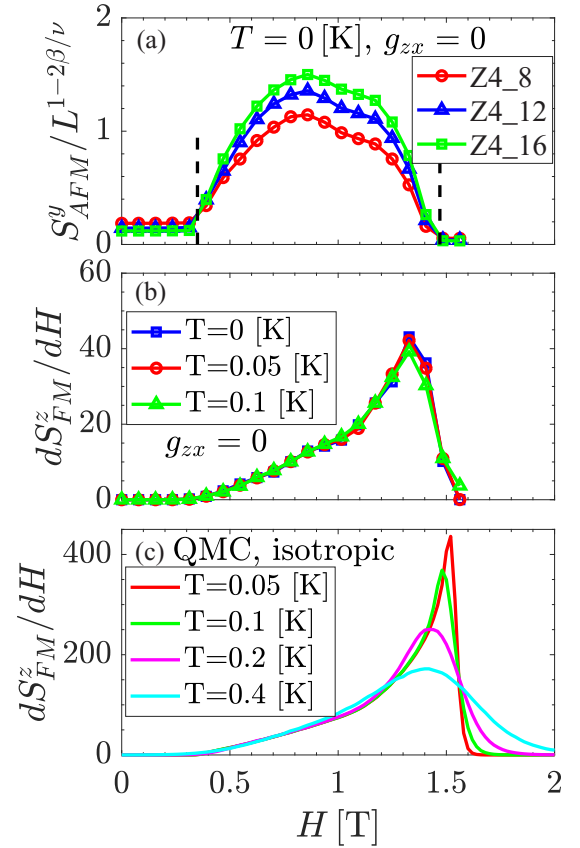

FIG. 7. (a) Similar to Fig. 3, but for the system without a tiny field in spin X direction, i.e., $g_{zx} = 0$. Two crossings occur at $H_{c_1} \sim 0.4$ T and $H \sim 1.4$ T. (b) Similar to Fig. 5(b) for "Z4_12" system, but for the model with $g_{zx} = 0$. The slope changes manifested in dS_{FM}^z/dH vs H suggest that a tiny g_{zx} is not necessary to explain the similar feature in ultrasound velocity in the experiment [17]. (c) QMC simulation results for a 16×16 honeycomb lattice with 512 sites without any anisotropy, i.e., $\lambda = 0$ and $g_{zx} = 0$.

First we do a ground-state ($T = 0$) finite-size scaling analysis for the same model without a staggered field in spin x, i.e., $g_{zx} = 0$ in Fig. 7(a). As expected, the crossing point occurs at $H \sim 1.5$ T (close to H_{c_2}) instead of happening at $H_{c_m} \sim 1.07$ T in the original model with $g_{zx} = 1/500$. Thus it coincides with the bottom-right edge of the dome computed from our finite-temperature calculations.

Next we examine dS_{FM}^z/dH for $g_{zx} = 0$ in Fig. 7(b). The slope changes observed in Fig. 5 appear quite similar to the $g_{zx} = 0$ case, and are again analogous to the slope changes in the ultrasound velocity signaling the vertical phase boundary in the experiment [17]. All the evidence above implies that the model with a tiny staggered magnetic field in spin X direction (nonzero g_{zx}) can give rise to an intermediate phase only at $T = 0$ and very small values of T. Such a model is therefore not able to explain the vertical H_m line observed in the experiment within the interpretation of this line being a true phase transition. The vertical phase boundary suggested by the ultrasound velocity in the experiment (or the derivative of FM structure factor) is more likely to be a crossover instead.

Finally, we investigated the fully isotropic model, where both $g_{zx} = 0$ and $\lambda = 0$ in Fig. 7(c). In this case, QMC can be

applied without encountering a sign problem [28]. dS_{FM}^z/dH is shown for the fully isotropic case on a $16 \times 16 \times 2$ lattice in Fig. 5(c). Inside the BEC dome we indeed also observe two different regimes. For $0.5T \lesssim H \lesssim 1.0T$, dS_{FM}^z/dH is only weakly dependent on temperature, while for $1.0T \lesssim H \lesssim 1.5T$ we observe that the peak close to the saturation field only develops at lower temperatures. This behavior is exactly what is observed in experiments by measuring the Bragg peaks and ultrasound velocity. Thus, the occurrence of two regimes in the magnetization process is intrinsic to the isotropic breathing honeycomb antiferromagnet and not necessarily related to an anisotropy in either the spin-spin interactions or the coupling to an external field.

VII. DISCUSSION AND CONCLUSIONS

We have investigated the finite-temperature phase diagram and thermodynamics of the "breathing" honeycomb lattice quantum dimer magnet in the parameter regime relevant to recent experiments on $Yb_2Si_2O_7$. We considered the effects of a small anisotropy in both the exchange coupling as well as the g tensor, proposed as an explanation for the occurrence for two regimes inside antiferromagnetic regime in the Bose-Einstein condensation dome of $Yb_2Si_2O_7$ [18].

Our simulations employing the METTS technique yield close agreement with the experimentally observed data. By detecting maxima in the specific heat and performing finite-size scaling analysis of antiferromagnetic structure factors, we have mapped out the extent of the Bose-Einstein condensation dome, which is found to closely track the experimentally observed data. Within the dome, two regimes have been distinguished in experiments by a change in the field dependence of the magnetization and the related ultrasound velocity measurements. This behavior is also found to be captured by the breathing honeycomb dimer model for which we observe a change of slope in the derivative of the ferromagnetic structure factor. Also we find close agreement when relating this quantity to the observed Bragg peak intensity and the related ultrasonic velocity measurements.

Our simulation data for specific heat Fig. 4 fits the experimental data well for the full range of the magnetic field. The occurrence of a peak in the specific heat indicating a phase transition was pointed out in the experiment. However, this peak was only present in the lower-field regime of the BEC dome but absent in the higher-field regime, which was interpreted as another indication of two regimes. With the system sizes attainable using METTS we are at present unable to resolve sharp peaks, which would require simulating large fully two-dimensional geometries. Hence, the question whether or not a sharp peak in the specific heat is absent or present needs to be investigated further in future studies.

Moreover, we investigated to which extent anisotropies in the model are relevant to our findings. We confirm previous results that a small anisotropy in the g tensor, $g_{xz} = g_{zz}/500$, leads to a phase transition at magnetic fields smaller than the saturation field at $T = 0$ using DMRG. At temperatures above the anisotropy scale, however, this effect becomes negligible and we find that the actual phase transition is once again approximately concomitant with the saturation field. We conclude that the critical line in this model does not extend across the full temperature range of the Bose-Einstein condensation dome. The change in slope of the magnetization an the magnetic structure factor at finite temperatures within the BEC dome is found to be a generic property occurring even in the fully isotropic case and is not related to a phase transition induced by the anisotropy.

[1] C. Lacroix, P. Mendels, and F. Mila (eds.) *Introduction to Frustrated Magnetism*, Springer Series in Solid-State Sciences (Springer, New York, 2011).

[2] V. Zapf, M. Jaime, and C. D. Batista, Bose-Einstein condensation in quantum magnets, Rev. Mod. Phys. **86**, 563 (2014).

[3] L. Savary and L. Balents, Quantum spin liquids: A review, Rep. Prog. Phys. **80**, 016502 (2017).

[4] J. P. F. LeBlanc, A. E. Antipov, F. Becca, I. W. Bulik, G. K.-L. Chan, C.-M. Chung, Y. Deng, M. Ferrero, T. M. Henderson, C. A. Jiménez-Hoyos, E. Kozik, X.-W. Liu, A. J. Millis, N. V. Prokof'ev, M. Qin, G. E. Scuseria, H. Shi, B. V. Svistunov, L. F. Tocchio, I. S. Tupitsyn *et al.* (Simons Collaboration on the Many-Electron Problem), Solutions of the Two-Dimensional Hubbard Model: Benchmarks and Results from a Wide Range of Numerical Algorithms, Phys. Rev. X **5**, 041041 (2015).

[5] J. I. Cirac, D. Pérez-García, N. Schuch, and F. Verstraete, Matrix product states and projected entangled pair states: Concepts, symmetries, theorems, Rev. Mod. Phys. **93**, 045003 (2021).

[6] A. Wietek, R. Rossi, F. Šimkovic, M. Klett, P. Hansmann, M. Ferrero, E. M. Stoudenmire, T. Schäfer, and A. Georges, Mott Insulating States with Competing Orders in the Triangular Lattice Hubbard Model, Phys. Rev. X **11**, 041013 (2021).

[7] Q.-R. Zhao, M.-J. Sun, Z.-X. Liu, and J. Wang, Magnon condensation in dimerized antiferromagnets with spin-orbit coupling, Phys. Rev. B **105**, 094401 (2022).

[8] Y. Sasago, K. Uchinokura, A. Zheludev, and G. Shirane, Temperature-dependent spin gap and singlet ground state in $BaCuSi_2O_6$, Phys. Rev. B **55**, 8357 (1997).

[9] M. Jaime, V. F. Correa, N. Harrison, C. D. Batista, N. Kawashima, Y. Kazuma, G. A. Jorge, R. Stern, I. Heinmaa,

S. A. Zvyagin, Y. Sasago, and K. Uchinokura, Magnetic-Field-Induced Condensation of Triplons in Han Purple Pigment $BaCuSi_2O_6$, Phys. Rev. Lett. **93**, 087203 (2004).

[10] C. Rüegg, D. F. McMorrow, B. Normand, H. M. Rønnow, S. E. Sebastian, I. R. Fisher, C. D. Batista, S. N. Gvasaliya, C. Niedermayer, and J. Stahn, Multiple Magnon Modes and Consequences for the Bose-Einstein Condensed Phase in $BaCuSi_2O_6$, Phys. Rev. Lett. **98**, 017202 (2007).

[11] H. Tanaka, A. Oosawa, T. Kato, H. Uekusa, Y. Ohashi, K. Kakurai, and A. Hoser, Observation of field-induced transverse Néel ordering in the spin gap system $TlCuCl_3$, J. Phys. Soc. Jpn. **70**, 939 (2001).

[12] C. Rüegg, N. Cavadini, A. Furrer, H. U. Güdel, K. Krämer, H. Mutka, A. Wildes, K. Habicht, and P. Vorderwisch, Bose-Einstein condensation of the triplet states in the magnetic insulator $TlCuCl_3$, Nature (London) **423**, 62 (2003).

[13] F. Yamada, T. Ono, M. Fujisawa, H. Tanaka, and T. Sakakibara, Magnetic-field induced quantum phase transition and critical behavior in a gapped spin system $TlCuCl_3$, J. Magn. Magn. Mater. **310**, 1352 (2007).

[14] T. Nakajima, H. Mitamura, and Y. Ueda, Singlet ground state and magnetic interactions in new spin dimer system $Ba_3Cr_2O_8$, J. Phys. Soc. Jpn. **75**, 054706 (2006).

[15] A. A. Aczel, Y. Kohama, M. Jaime, K. Ninios, H. B. Chan, L. Balicas, H. A. Dabkowska, and G. M. Luke, Bose-Einstein condensation of triplons in $Ba_3Cr_2O_8$, Phys. Rev. B **79**, 100409(R) (2009).

[16] M. Kofu, H. Ueda, H. Nojiri, Y. Oshima, T. Zenmoto, K. C. Rule, S. Gerischer, B. Lake, C. D. Batista, Y. Ueda, and S.-H. Lee, Magnetic-Field Induced Phase Transitions in a Weakly Coupled $s = 1/2$ Quantum Spin Dimer System $Ba_3Cr_2O_8$, Phys. Rev. Lett. **102**, 177204 (2009).

[17] G. Hester, H. S. Nair, T. Reeder, D. R. Yahne, T. N. DeLazzer, L. Berges, D. Ziat, J. R. Neilson, A. A. Aczel, G. Sala, J. A. Quilliam, and K. A. Ross, Novel Strongly Spin-Orbit Coupled Quantum Dimer Magnet: $Yb_2Si_2O_7$, Phys. Rev. Lett. **123**, 027201 (2019).

[18] M. O. Flynn, T. E. Baker, S. Jindal, and R. R. P. Singh, Two Phases Inside the Bose Condensation Dome of $Yb_2Si_2O_7$, Phys. Rev. Lett. **126**, 067201 (2021).

[19] S. R. White, Density Matrix Formulation for Quantum Renormalization Groups, Phys. Rev. Lett. **69**, 2863 (1992).

[20] U. Schollwöck, The density-matrix renormalization group in the age of matrix product states, Ann. Phys. **326**, 96 (2011).

[21] S. R. White, Minimally Entangled Typical Quantum States at Finite Temperature, Phys. Rev. Lett. **102**, 190601 (2009).

[22] E. Stoudenmire and S. R. White, Minimally entangled typical thermal state algorithms, New J. Phys. **12**, 055026 (2010).

[23] A. Wietek, Y.-Y. He, S. R. White, A. Georges, and E. M. Stoudenmire, Stripes, Antiferromagnetism, and the Pseudogap in the Doped Hubbard Model at Finite Temperature, Phys. Rev. X **11**, 031007 (2021).

[24] C. Feng, A. Wietek, E. M. Stoudenmire, and R. R. P. Singh, Order, disorder, and monopole confinement in the spin-$\frac{1}{2}$ XXZ model on a pyrochlore tube, Phys. Rev. B **106**, 075135 (2022).

[25] M. Fishman, S. R. White, and E. M. Stoudenmire, The ITensor software library for tensor network calculations, SciPost Phys. Codebases 4 (2022).

[26] J. Haegeman, C. Lubich, I. Oseledets, B. Vandereycken, and F. Verstraete, Unifying time evolution and optimization with matrix product states, Phys. Rev. B **94**, 165116 (2016).

[27] H. Suwa and S. Todo, Markov Chain Monte Carlo Method without Detailed Balance, Phys. Rev. Lett. **105**, 120603 (2010).

[28] S. Todo, worms: A simple worm code, https://github.com/wistaria/worms (2022).

[29] C. Feng, H. Guo, and R. T. Scalettar, Charge density waves on a half-filled decorated honeycomb lattice, Phys. Rev. B **101**, 205103 (2020).

[30] C. Feng and R. T. Scalettar, Interplay of flat electronic bands with Holstein phonons, Phys. Rev. B **102**, 235152 (2020).

[31] Y. Zhang, C. Feng, R. Mondaini, G. G. Batrouni, and R. T. Scalettar, Charge singlets and orbital-selective charge density wave transitions, Phys. Rev. B **106**, 115120 (2022).

[32] C. Kvande, C. Feng, F. Hébert, G. G. Batrouni, and R. T. Scalettar, Enhancement of charge density wave correlations in a Holstein model with an anharmonic phonon potential, arXiv:2303.13708.